BIOCHEMISTRY
including biophysical chemistry & molecular biology
Article

Biochemistry **2010,** *49,* 9457–9469 9457
DOI: 10.1021/bi100077x

Structural Characterization of GNNQQNY Amyloid Fibrils by Magic Angle Spinning NMR[†]

Patrick C. A. van der Wel,[‡] Józef R. Lewandowski,[§] and Robert G. Griffin*

Francis Bitter Magnet Laboratory and Department of Chemistry, Massachusetts Institute of Technology, Cambridge, Massachusetts 02139. [‡]Current address: Department of Structural Biology, University of Pittsburgh School of Medicine, Pittsburgh, PA 15260 [§]Current address: Université de Lyon, CNRS/ENS-Lyon/UCB Lyon 1, Centre de RMN à Très Hauts Champs, 5 rue de la Doua, 69100 Villeurbanne, France

Received January 17, 2010; Revised Manuscript Received July 15, 2010

ABSTRACT: Several human diseases are associated with the formation of amyloid aggregates, but experimental characterization of these amyloid fibrils and their oligomeric precursors has remained challenging. Experimental and computational analysis of simpler model systems has therefore been necessary, for instance, on the peptide fragment $GNNQQNY_{7-13}$ of yeast prion protein Sup35p. Expanding on a previous publication, we report here a detailed structural characterization of GNNQQNY fibrils using magic angle spinning (MAS) NMR. On the basis of additional chemical shift assignments we confirm the coexistence of three distinct peptide conformations within the fibrillar samples, as reflected in substantial chemical shift differences. Backbone torsion angle measurements indicate that the basic structure of these coexisting conformers is an extended β-sheet. We structurally characterize a previously identified localized distortion of the β-strand backbone specific to one of the conformers. Intermolecular contacts are consistent with each of the conformers being present in its own parallel and in-register sheet. Overall the MAS NMR data indicate a substantial difference between the structure of the fibrillar and crystalline forms of these peptides, with a clearly increased complexity in the GNNQQNY fibril structure. These experimental data can provide guidance for future work, both experimental and theoretical, and provide insights into the distinction between fibril growth and crystal formation.

There are more than 20 human diseases, include the Alzheimer's, Parkinson's, and Huntington's diseases (*1*), that are associated with the formation of amyloid fibrils through the misfolding and aggregation of different amyloidogenic proteins. To further our understanding of these diseases, which affect increasingly large fractions of the population, it is essential to understand the misfolding process in terms of the mechanism of fibril formation as well as the structural features of the resulting aggregates. Unfortunately, it has proven challenging to obtain structural information on the highly stable, noncrystalline amyloid or amyloid-like fibrils, because they do not diffract to high resolution and are insoluble. Thus, the two major techniques used in structural biology, X-ray diffraction and solution NMR, are not applicable to these systems. The steps that constitute the misfolding process itself are even more difficult to examine experimentally. This includes the structure determination of oligomers that are thought to form precursors to the fibrillar form and are increasingly suspected to be toxic species in amyloid-related disorders. Obtaining structural information on these systems often relies on a combination of indirect methods (*2*). The paucity of experimental data has stimulated a significant interest in exploring theoretical or computational studies of fibril formation and the intermediates formed along the pathway to mature fibrils (*3*).

Many computational studies aim to understand amyloid formation by focusing on relatively simple model systems that should represent the essential features of amyloid fibril structure. Recently, experimental atomic level data on an amyloid core structure were obtained via X-ray crystallography on a crystalline (i.e., nonfibrillar) form of a fibril-forming peptide, GNNQQNY (*4*, *5*). This peptide is one of various peptide fragments from the yeast prion protein Sup35p that have been found to form amyloid-like fibrils, but this is one that also forms microcrystals (*6*). With newly developed microdiffractometers, these crystals yielded a high-resolution structure, and the short length of the peptide and the relative simplicity of the cross-β spine motif present in the crystals have made it an attractive model amyloid fibril system. As such, it has featured in numerous *in silico* studies of the characteristics and formation of model amyloid fibrils (*7*−*27*). The purpose of such simulations is to produce insights into the common features of the fibril formation process. This specifically includes information on unstable intermediates, thereby complementing experimental data that is most easily obtained on the more stable states along the fibril formation pathway. Note that such intermediates are of particular interest due to their potential role as toxic agents (*28*).

However, it is important to keep in mind that the widely used structural data on GNNQQNY are based on the *crystalline form* of the peptide and that the same peptide also forms amyloid fibrils under very similar conditions (*6*, *29*, *30*). In electron micrographs these latter moieties have a striated, flat ribbon-like appearance (*29*, *30*), similar to fibrils formed by other peptides

[†]This research was supported by the National Institutes of Health through Grants EB-003151 and EB-002026.

*Corresponding author: e-mail, rgg@mit.edu; phone, (617) 253-5597; fax, (617) 253-5405.

Published on Web 08/09/2010

and proteins (*31*−*36*). Experimental studies have indicated significant structural differences between the crystalline and fibrillar structures (*30*, *37*). Given the interest in GNNQQNY as a model system of *fibril* formation, it is important to characterize the molecular structure of these fibrils and compare them to the crystal structure, an experimental challenge for which few techniques are available. Magic angle spinning (MAS)[1] NMR has proved uniquely valuable in the structural characterization of amyloid fibrils (*38*, *39*) due to its ability to provide site-specific structural constraints on biological solids without requiring crystalline samples.

Accordingly, we have previously used MAS NMR to obtain initial qualitative data comparing the GNNQQNY crystals and fibrils, which revealed significant differences in chemical shifts between the two forms, suggestive of differences in atomic structure (*30*). In addition, the fibrils featured three distinct peptide conformations, which differ among themselves in terms of their chemical shifts. However, the data were semiquantitative and limited to the few N-terminal residues which were labeled in the fibrils. Within those sites the MAS NMR results suggested a localized helix-like deviation from β-sheet structure for one of these conformers, in contrast to more typical amyloid β-sheet structures (as were found in the other two fibril forms). As such, the nature and structure of these conformers have remained a surprising and poorly understood aspect of these a priori (and based on the X-ray data) seemingly simple peptide fibrils.

To clarify this situation and provide further details on the structure of the GNNQQNY fibrils, we performed additional MAS NMR experiments on more extensively labeled fibril samples. Thus, we present here more complete chemical shift assignments and structural NMR measurements. Our experiments reveal that all three conformers basically have a β-sheet conformation, based on both chemical shift analysis and backbone torsion angle measurements that relate the relative orientations of $^{13}C-^{15}N$ dipolar interaction vectors (*40*). The previously observed chemical shift deviations for the second fibril form reflect a localized backbone distortion rather than a completely non-β monomer structure. We also examine the arrangement of monomers within these β-sheets by measuring intermolecular $^{13}C-^{13}C$ and $^{13}C-^{15}N$ distance measurements. $^{13}C-^{13}C$ double quantum techniques (*41*) can generate coherences between singly ^{13}C-labeled carbonyl sites in neighboring peptide monomers and allows one to measure the $^{13}C{=}O{-}{-}{-}^{13}C{=}O$ distance to help constrain the strand−strand arrangement within amyloid fibrils (*42*−*46*). Rotational resonance width (R^2W) measurements (*47*, *48*) are used to determine additional intermolecular $^{13}C-^{13}C$ distances (*49*−*51*) in an approach recently used in other peptides and proteins (*52*−*54*). A mixture of singly ^{15}N- and ^{13}C-labeled peptides was used to determine $^{13}C-^{15}N$ distances via 1D REDOR (*55*) and 2D TEDOR (*56*, *57*) experiments. Note that analogous $^{13}C-^{13}C$ and $^{13}C-^{15}N$ experiments have been used for the identification of interstrand contacts in other amyloids (*58*−*60*). These intermolecular distance measurements consistently show that the Gly-7 residue of different monomers is in close proximity and that G7−G7 intermolecular interactions *only* occur between identical fibril conformers (i.e., not between different conformers). $^{13}C-^{13}C$ proton-assisted recoupling (PAR) experiments (*61*) reveal similar same-to-same contacts elsewhere along the sequence. Taken together, these data point to the different fibril conformers each adopting an in-register parallel (IP) structure, somewhat analogous to the crystals. Nonetheless, our data also show that significant chemical shift differences are present between the crystals and fibrils. Some of these correlate clearly to differences in backbone conformation between the fibril forms, in contrast to the two crystalline structures that feature virtually identical backbone (and side chain) conformations. We examine these differences with the crystals and discuss the implications for past and future computational studies on this model system and its formation of amyloid fibrils.

EXPERIMENTAL PROCEDURES

Sample Preparation. GNNQQNY crystalline and fibrillar samples were prepared as described previously (*30*). The peptides were prepared by solid-phase peptide synthesis at CS Bio Inc. (Menlo Park, CA) and New England Peptide (Gardner, MA) and were isotopically labeled with ^{13}C- and/or ^{15}N-labeled amino acids from Cambridge Isotope Laboratories (Andover, MA). Various differently labeled peptides were prepared, including segmentally and site-specifically labeled versions. Crystal and fibril formation was accomplished by rapid dissolution of the lyophilized peptide in water, resulting in an acidic peptide solution. Largely as a function of concentration, the peptides form monoclinic or orthorhombic crystals and/or fibrils (*29*, *30*). After centrifugation and removal of excess water, the peptide aggregates were packed into MAS rotors (Revolution NMR, Fort Collins, CO). The samples were maintained in a hydrated state at all times and were stored at 4 °C.

NMR Methods. (*A*) *Assignment Methods*. NMR measurements were performed using custom-made spectrometers (designed by D. J. Ruben, Francis Bitter Magnet Laboratory, MIT) operating at ^1H Larmor frequency $\omega_{H0}/2\pi$ = 500 MHz (11.7 T), and $\omega_{H0}/2\pi$ = 700 MHz (16.4 T). Experiments at 500 MHz utilized a Varian triple-resonance HCN probe equipped with a 4 mm stator, whereas experiments at 700 MHz used Varian triple-resonance HCN probes with a 3.2 mm MAS stator outfitted with either a solenoid or scroll coil (Varian Inc., Palo Alto, CA) (*62*). Spinning was regulated with Bruker MAS I spinning frequency controllers (Bruker BioSpin, Billerica MA). Assignment experiments used methods similar to those described previously (*30*). $^{13}C-^{13}C$ 2D assignment spectra were obtained using DARR/RAD (*63*, *64*) or PAR (*65*) mixing. $^{15}N-^{13}C$ correlations were obtained using double CP-based measurements (*66*) to give NCA, NCO, NCOCX, and NCACX 2D and 3D spectra (*67*−*69*). The NCOCX and NCACX (*70*) pulse sequences included a 10−20 ms DARR/RAD period to establish the intraresidue $^{13}C-^{13}C$ correlations. TPPM ^1H decoupling (*71*) was applied during acquisition and t_1 evolution. ^{13}C chemical shifts were referenced to aqueous DSS using external referencing via the published ^{13}C chemical shifts of adamantane (*72*). ^{15}N chemical shifts were referenced to liquid ammonia via indirect referencing using the suggested IUPAC frequency ratios ($^{13}C/^1H$) of aqueous DSS and liquid NH_3 ($^{15}N/^1H$) (*73*, *74*). NMR data processing and assignment were done with the aid of the NMRPipe (*75*), Sparky (*76*), and CCPNMR/Analysis (*77*) software packages.

(*B*) *Torsion Angle Measurements*. Chemical shift based backbone torsion angle analysis was performed with the TALOS

[1]Abbreviations: CSI, chemical shift indexing; DQ, double quantum; DRAWS, dipolar recoupling with a windowless sequence; IP, in-register parallel; MAS, magic angle spinning; R^2, rotational resonance; R^2W, rotational resonance width; REDOR, rotational echo double resonance; SQ, single quantum; TEDOR, transferred echo double resonance; TPPM, two-pulse phase modulation.

program (version 2003.027.13.05) (*78*) using the default database of 78 proteins. The results were examined by hand to evaluate individual cases. To resolve inconclusive cases, and to provide more precise results, complementary measurements of the Ψ angles were done via NCCN torsion angle experiments (*40*, *79*), which applied REDOR dephasing of ^{13}C double-quantum coherence obtained with the SPC5 pulse sequence (*80*). Data fitting was done using the numerical simulation software SPINEVOLUTION (*81*), employing secondary constraints (bond distances and bond angles) as determined from the crystal structure of the monoclinic crystals of GNNQQNY (*4*). Measurements on 100% [U-^{13}C,^{15}N-GNNQ]QNY and 100% GNN[U-^{13}C,^{15}N-QQNY] monoclinic crystals were done at $\omega_{0H}/2\pi$ = 500 MHz, and measurements on 100% [U-^{13}C,^{15}N-GNNQ]QNY and 100% GNN-[U-^{13}C,^{15}N-QQN]Y fibrils were done at $\omega_{0H}/2\pi$ = 700 MHz. Note that the higher magnetic field was essential to allow the distinct conformers within the fibrils to be resolved (*30*). The Supporting Information contains pulse sequence schematics and additional experimental details for these as well as subsequent MAS NMR experiments.

(*C*) *Intermolecular Distance Measurements*. DQ DRAWS (dipolar recoupling with a windowless sequence) experiments (*41*, *44*−*46*) were aimed at establishing strand−strand contacts characteristic of IP sheets by detecting the buildup of DQ-filtered coherence buildup in GNNQQNY fibrils and crystals containing a single ^{13}C-carbonyl-labeled residue, [^{13}C′-Gly]. The experiments were performed at $\omega_{0H}/2\pi$ = 500 MHz using a 4 mm Varian HCN probe. The resulting buildup curves were analyzed by fitting with the numerical simulation package SPINEVOLUTION (*81*), employing a linear spin system consisting of seven ^{13}C sites. These CPU-intensive calculations were performed on the 156-core Beowulf cluster at the Department of Structural Biology (University of Pittsburgh).

Fibril samples were prepared from 50/50 mixtures of specifically labeled [^{13}C′-Gly]-NNQQNY and [^{15}N-Gly]-NNQQNY. REDOR was used to measure intermolecular distances between these labels, using 3.2 mm Varian MAS probes at $\omega_{0H}/2\pi$ = 700 MHz. ^{15}N and ^{13}C observed measurements were done using a Varian solenoid HCN probe at a MAS rate $\omega_r/2\pi$ = 8 kHz and employing sample cooling with −8 °C cooling gas. We used a REDOR mixing period of up to 25 ms with a 4 s recycle delay, 91 kHz TPPM ^{1}H decoupling (*71*) during mixing, evolution, and acquisition, and 50 kHz REDOR pulses (on ^{13}C when observing ^{15}N and reversed). Extended mixing time (up to 50 ms) REDOR measurements were performed using a scroll-coil BioMAS probe (Varian Inc., Palo Alto, CA), observing ^{13}C. Data fitting and simulation of these REDOR curves were accomplished with SPINEVOLUTION (*81*) by simulating the normalized S/S_0 data (i.e., in the absence of relaxation), where S_0 data were obtained experimentally with the same mixing time but without the application of REDOR pulses. To supplement these 1D experiments, a single 2D *z*-filtered TEDOR (*57*) spectrum with 16 ms mixing time was recorded.

To measure the intermolecular ^{13}C−^{13}C distance in 50/50 mixed [^{13}C′-Gly]-NNQQNY and [^{13}Cα-Gly]-NNQQNY fibril samples, we used rotational resonance (R^2) width measurements (*47*), implemented as described previously (*52*). These spectra were recorded at $\omega_{0H}/2\pi$ = 700 MHz using a Varian solenoid HCN probe with a 3.2 mm spinner. A series of 2D spectra was recorded at different MAS rates using a constant 30 ms R^2 mixing time, with 95 kHz TPPM ^{1}H decoupling (*71*). These measurements were done near $\omega_r/2\pi$ = ∼11 kHz to match the n = 2 R^2 conditions between the Gly C′ and Gly Cα sites. At each MAS rate the peak intensities for C′−Cα cross-peaks were measured and scaled relative to C′ intensities of reference data with 0 ms R^2 mixing time. The resulting R^2W profiles were fit with a multipole-multimode Floquet theory based program (*52*) to determine the distances.

Table 1: Assignment of MAS NMR Resonances for the Three Predominant Conformers Found in GNNQQNY Fibrils[a]

		^{13}C chemical shift (ppm)					^{15}N chemical shift (ppm)		
		C′	C_α	C_β	C_γ	C_δ	N	N_δ	N_ε
fibril form 1	Gly_7	171.2	43.5				27.6		
	Asn_8	172.8	53.0	39.7	177.3		121.1	114.0	
	Asn_9	173.5	52.7	40.4	176.4		123.0	114.5	
	Gln_{10}	176.5	55.0	34.0	34.7	180.8	123.3		114.3
	Gln_{11}	174.8	55.2	34.4	34.5	179.2	121.9		114.2
	Asn_{12}	172.5	53.3	41.4	173.9		124.2	115.4	
fibril form 2	Gly_7	170.6	44.1				27.4		
	Asn_8	173.8	56.0	37.3	178.5		113.2	112.0	
	Asn_9	176.0	53.3	39.2	176.2		116.8	113.5	
	Gln_{10}	174.8	54.0	33.4	33.3	178.2	117.5		112.0
	Gln_{11}	174.1	54.6	32.4	34.1	179.9	121.8		111.3
	Asn_{12}	173.1	49.8	43.1	180.8		127.1	110.2	
fibril form 3	Gly_7	170.1	43.4				27.5		
	Asn_8	174.2	52.6	40.1	177.0		118.6	115.2	
	Asn_9	173.3	53.7	42.6	176.2		121.3	115.5	
	Gln_{10}	174.8	54.7	32.5	34.2	180.8	127.1		114.5
	Gln_{11}	175.0	53.8	36.2	35.2	180.0	118.2		116.9
	Asn_{12}	173.6	52.6	40.6	174.3		123.3	114.6	

[a]These assignments are based on various SSNMR assignment measurements performed at $\omega_{0H}/2\pi$ = 700 MHz. The uncertainty in the chemical shifts is estimated to be ∼0.25 ppm.

Fibrils were also prepared from approximately equal amounts of GN[U-^{13}C,^{15}N-N]QQNY and GNN[U-^{13}C,^{15}N-Q]QNY, which were studied at $\omega_{0H}/2\pi$ = 700 MHz with a 2D ^{13}C−^{13}C PAR experiment with τ_{mix} = 14 ms (*65*) and a 2D ^{13}C−^{13}C DARR correlation experiment with τ_{mix} = 10 ms, both at $\omega_r/2\pi$ = 9.5 kHz.

RESULTS

Solid-State NMR Assignments. We have previously described the partial chemical shift assignments of the three coexisting fibril forms of GNNQQNY based on several samples where the first four residues (GNNQ) were uniformly ^{13}C,^{15}N-labeled. This allowed for some initial insight into the fibril dynamics and structure. We now present additional results on a peptide that has a subsequent segment ^{13}C,^{15}N-labeled (GNN-[U-^{13}C,^{15}N-QQN]Y). We used standard 2D and 3D homo- and heteronuclear methods to obtain complete assignments on the labeled residues, the results of which are summarized in Table 1, together our previously published data (*30*). We relied on 3D NCACX and NCOCX experiments to resolve various heavily overlapped resonances. Slices from these 3Ds, along with further experimental details, are included in the Supporting Information. Figure 1 contains 2D NCO spectra obtained for the crystalline and fibrillar forms of the peptide. The figure demonstrates that the shifts of the fibrillar peptides vary substantially from their crystalline counterparts and shows the multiplicity that is due to the coexistence of three distinct peptide conformers within the fibrillar sample. The intensity variations between the fibril resonances, which can be correlated to differences in their population

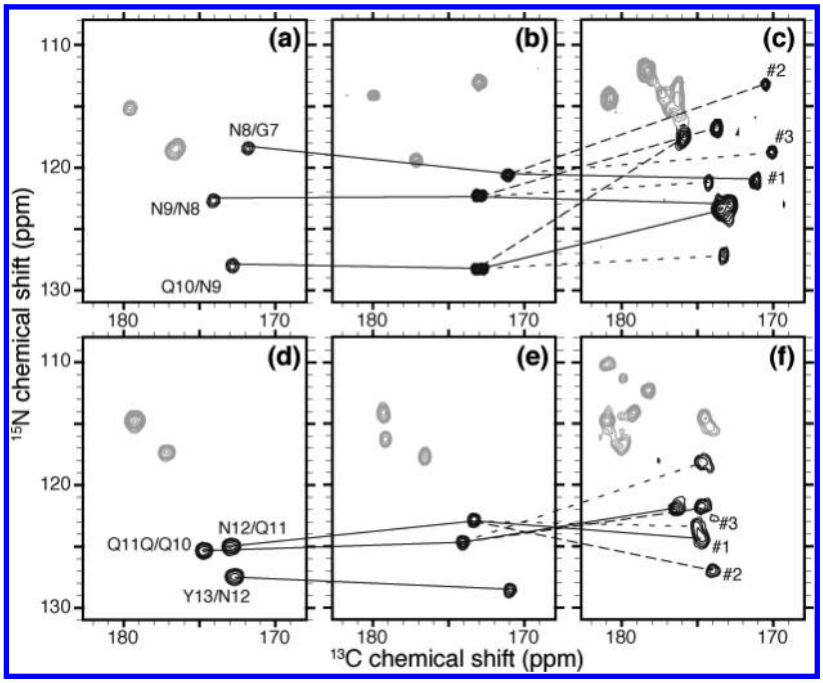

FIGURE 1: MAS NMR $^{15}N^{13}CO$ spectra on (a, b) [U-^{13}C,^{15}N-GNNQ]QNY monoclinic and orthorhombic crystals and (c) fibrils, as well as (d, e) GNN[U-^{13}C,^{15}N-QQNY] monoclinic and orthorhombic crystals and (f) GNN[U-^{13}C,^{15}N-QQN]Y fibrils. All data were acquired at $\omega_{0H}/2\pi$ = 700 MHz except (a) and (d) which were acquired at 500 MHz. Backbone cross-peaks connecting neighboring residues are highlighted in black and connected between panels. The chemical shifts of the two crystalline forms were found to be similar, but the fibrils exhibit significantly different chemical shifts and contain three conformers (marked #1−#3), which vary in intensity as well as chemical shift.

Table 2: CSI and TALOS-Based Torsion Angle Data for GNNQQNY Fibrils[a]

	fibril conformer 1			fibril conformer 2			fibril conformer 3		
	TALOS			TALOS			TALOS		
residue	ϕ/deg	ψ/deg	CSI	ϕ/deg	ψ/deg	CSI	ϕ/deg	ψ/deg	CSI
G7	*	*	β	*	*	β	*	*	β
N8	−108 ± 20	127 ± 10	β	54 ± 6	40 ± 13	α	−119 ± 18	131 ± 12	β
N9	−101 ± 11	131 ± 13	β	−88 ± 22	X	α	−116 ± 19	128 ± 8	β
Q10	−131 ± 14	151 ± 13	β	−142 ± 13	156 ± 10	β	−146 ± 15	155 ± 15	β
Q11	−150 ± 12	149 ± 12	β	−129 ± 22	132 ± 11	β	−145 ± 12	153 ± 9	β
N12	*	*	β	*	*	β	*	*	β

[a]Some of these data were previously reported (*30*). Asterisks indicate data at the termini of the peptide that are unsuitable for TALOS analysis, since it relies on triplets of residues. The data for Asn-9 in fibril form 2 were inconclusive (marked with X; see also Supporting Information Figure S5). More CSI data analysis is included in the Supporting Information (Figure S4).

and local dynamical variations, agree with our earlier observations on the other residues.

TALOS Torsion Angle Analysis. The observed chemical shifts were used to determine the secondary structure and backbone torsion angles. Chemical shift indexing (CSI) (*82*, *83*) provides a qualitative analysis of the secondary structure and indicated a predominantly β-sheet conformation (see Table 2 and the Supporting Information). The assignment data were also used to determine the backbone torsion angles in a more quantitative manner, employing the widely used TALOS software package (*78*) that compares observed chemical shifts with those of known protein structures. Despite being based on solution NMR shifts of mostly globular proteins, this approach proved reasonably reliable for the monoclinic crystals (*30*). It also seems to work well for most, but not for all, residues in the fibril conformers. In particular for residue N9 it proved problematic for the TALOS analysis to provide a clear answer (Supporting Information Figure S5). While we can identify a single constrained backbone conformation for forms 1 and 3, no unequivocal solution is found for conformer 2. The TALOS results are tabulated in Table 2, and further details are included in the Supporting Information. Analogous to the CSI data, conformers 1 and 3 are consistently β-sheet, while conformer 2 may feature an ill-defined distortion from an extended β-sheet conformation.

NCCN Torsion Angle Measurements. To verify the TALOS analysis and determine the backbone conformation of additional residues (e.g., the N-terminal Gly that are not suitable for TALOS analysis), we also performed NCCN torsion angle measurements. These rely on the generation of DQ coherence between the backbone carbons of residue i, which is then dephased under the influence of the $^{13}C-^{15}N$ dipolar interactions involving the ^{15}N sites of the i and $i+1$ residues (*40*). As reference data, we first performed these measurements on monoclinic crystals prepared from segmentally labeled GNNQQNY peptides. Figure 2a shows a representative 2D spectrum, illustrating

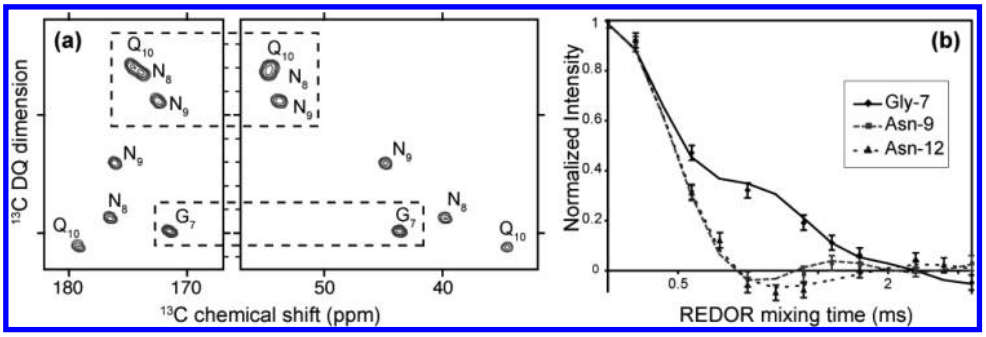

FIGURE 2: Representative NCCN torsion angle data on GNNQQNY monoclinic crystals, obtained at $\omega_{0H}/2\pi$ = 500 MHz. (a) 2D reference spectrum on 100% [U-^{13}C,^{15}N-GNNQ]QNY crystals, without REDOR dephasing, showing the assignments of the signals. Boxed cross-peaks are due to backbone sites, which were used for Ψ torsion angle measurements. Other signals reflect Asn and Gln side chains. (b) Experimental dephasing curves as a function of the REDOR mixing time for three residues (G7, N9, and N12). The solid lines indicate best-fit simulations of the experimental data, obtained with SPINEVOLUTION (*81*).

Table 3: Backbone Torsion Angle ψ for Monoclinic Crystalline GNNQQNY[a]

residue	X-ray ψ/deg	TALOS ψ/deg	NCCN $\|\psi\|$/deg
G7	−162.2		162 (154−168)
N8	141.2	131 ± 10	151 (137−158)
N9	125.2	136 ± 9	122 (< 146)
Q10	112.8	126 ± 14	116 (87−136), 18 (< 64)
Q11	126.8	142 ± 15	117, 23 (< 139)
N12	97.7	119 ± 13	105, 44 (< 137)

[a]X-ray and TALOS data are literature values (*4*, *30*). Y13 is omitted since it has no defined ψ angle as the C-terminal residue. Multiple minima are listed where applicable, and uncertainty ranges are included in parentheses. In these cases the global minimum ("best fit") is listed first.

the assignments of the recoupled sites. Note that here the only sites of specific interest for the ψ torsion angle experiments are those involving the backbone carbons (indicated with dashed rectangles). The intensity of these cross-peaks was monitored as a function of the REDOR time, resulting in dephasing curves (e.g., Figure 2b). Numerical simulations of these experimental data were done with the SPINEVOLUTION program (*81*), in order to determine the ψ backbone torsion angles. The resulting ψ values are listed in Table 3, alongside the results from the TALOS analysis (*30*) and the X-ray crystallographic data (*4*). Note that the best-fit values are consistent with the TALOS results but are significantly closer to the X-ray values, suggesting an improved accuracy (see also Figure S7 in the Supporting Information and the discussion below).

Analogous NCCN measurements were performed on GNNQQNY fibril samples with overlapping segmental labeling: [U-^{13}C,^{15}N-GNNQ]QNY] and GNN[^{13}C,^{15}N-QQN]Y (Figure 3). Due to the multiple forms being present, we observe significant cross-peak overlap. Peak integrations were only done on cross-peaks that could be resolved or at least deconvoluted reliably. This meant that several sites were missing, but none of these involved data that were ambiguous or missing in the TALOS analysis (see Supporting Information). In addition, the fibril data had fewer mixing times and a generally poorer signal-to-noise ratio than the crystal data (in part due to the multiple conformations and broader line widths). Examplary results are illustrated in Figure 4 for the N9 residue, where the TALOS data were ambiguous (see Supporting Information Figure S5). Consistent with large differences in the chemical shift (and the CSI in Figure S3 of the Supporting Information), the NCCN dephasing curve for conformer 2 is significantly different from the other two fibril forms, corresponding to different ψ values (Figure 4b−d). In this case, both the NCCN and the TALOS results are somewhat ambiguous. However, the NCCN data clearly exclude several of the TALOS matches (panel e). The TALOS data had a large uncertainty in ψ, which we can now resolve, but was reasonably consistent in terms of the ϕ angle. Similar observations apply to N8, where fibril form 1 and the monoclinic crystals show similar dephasing, but the curve is quite different for conformer 2 (Supporting Information Figure S8). For form 2, the best solution occurs at the non-β torsion angles, which would explain the substantial chemical shift differences seen in this conformer's N-terminus (Figure 1) and the associated non-β CSI values (*30*). Although less consistent with all the available data (including the CSI and TALOS results), there is also a secondary and less likely solution that is closer to β-sheet torsion angles at φ, ψ ∼−80°, 117°.

By combining the NCCN results with the TALOS data, we obtained the unified backbone torsion angles summarized in Table 4 (see also Supporting Information). Note that many of these values (and their errors) basically reflect the TALOS results and that application of TALOS to the crystalline peptides suggests that the TALOS errors are likely to underestimate the true uncertainty (see Supporting Information and Discussion).

Intermolecular G7-G7 Backbone Contacts. We also performed experiments providing initial constraints for the supramolecular structure of the fibrils, initially targeting characteristic distances between the β-strands in an IP β-sheet. For the IP β-sheets found within the GNNQQNY crystals, the X-ray distance between subsequent peptide monomers is 4.9 Å (*4*, *5*), as is typical for amyloid fibrils. As reference data, we used DQ-filtered DRAWS (*41*, *44*−*46*) to measure the DQ-buildup in monoclinic crystals prepared from GNNQQNY in which a single carbonyl site is labeled (Gly-^{13}C′). Figure 5a shows the DQ signal (as a fraction of the cross-polarization signal) as a function of the DQ DRAWS mixing time. The presence of any significant intensity suggests that the ^{13}C′ sites must be in close proximity. Numerical simulation of the experimental data suggested a distance of 4.4 Å, which is in reasonably good agreement with the X-ray distance.

Identical measurements were performed on analogously labeled amyloid fibrils, as shown in Figure 5b. Since we were unable to reliably resolve the three individual fibril conformers at the 11.74 T field used in these experiments, the combined intensity was used for the fibril data analysis. A simple model that assumes an identical distance and relaxation for all three fibril forms results in a ^{13}C′−^{13}C′ distance of 4.9 Å (included in Table 5),

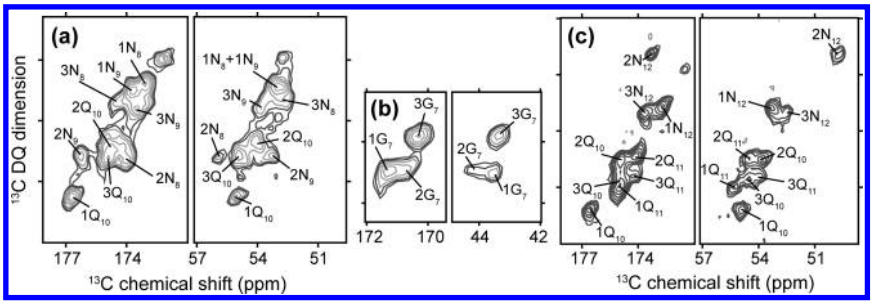

FIGURE 3: Assignments of fibril NCCN SQ-DQ 2D spectra. These are the reference data with 0 ms REDOR mixing time for (a, b) 100% [U-^{13}C,^{15}N-GNNQ]QNY and (c) GNN[U-^{13}C,^{15}N-QQN]Y fibrils. Panel b shows the spectral region with the G7 cross-peaks. Measurements were done at $\omega_{0H}/2\pi$ = 700 MHz. Note the intensity variations and the significant overlap of various signals.

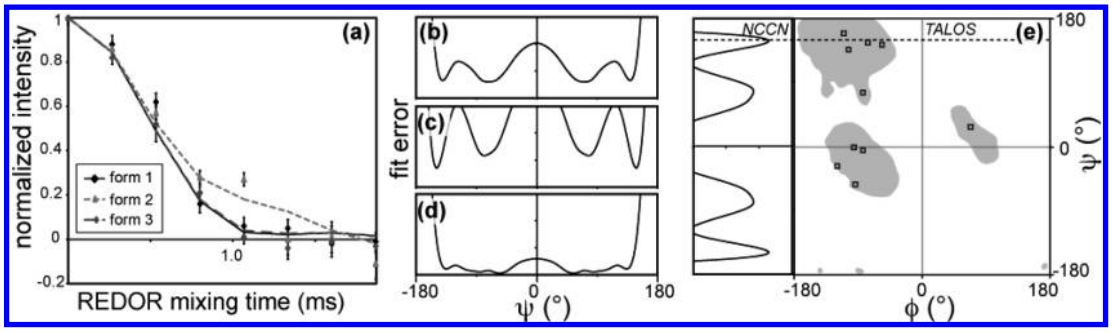

FIGURE 4: Complementary data from NCCN and TALOS torsion angle analyses. (a) Experimental and simulated NCCN dephasing data for N9 in fibril forms 1 (black diamonds and solid line), 2 (light gray triangles and dashed line), and 3 (dark gray diamonds and dashed line). The simulations of the experimental data result in fits that are consistent with multiple torsion angles: N9 in (b) form 1, (c) form 2, and (d) form 3. Nonetheless, these data exclude many of the ambiguous TALOS data, as illustrated in (e) for the NCCN fit (left) and the TALOS-based Ramachandran plot (right) of N9 in form 2. The dashed line indicates the solution most consistent with both data sets (shown as lines in panel a).

Table 4: Summary of MAS NMR-Based Torsion Angles in GNNQQNY Fibrils[a]

	fibril conformer 1		fibril conformer 2		fibril conformer 3	
residue	ϕ/deg	ψ/deg	ϕ/deg	ψ/deg	ϕ/deg	ψ/deg
G7	n/a	166 ± 10	n/a	166 ± 20	n/a	180 ± 13
N8	−108 ± 20	145 ± 20	54 ± 6[b]	40 ± 13[b]	−119 ± 18	131 ± 12
N9	−101 ± 11	136 ± 18	−88 ± 22	150 ± 13	−116 ± 19	130 ± 12
Q10	−131 ± 14	130 ± 15	−142 ± 13	135 ± 15	−146 ± 15	121 ± 20
Q11	−150 ± 12	136 ± 15	−129 ± 22	132 ± 11	−145 ± 12	153 ± 9
N12[c]	β	β	β	β	β	β

[a]The data include data determined from TALOS chemical shift analysis (Table 2), chemical shift index analysis, and Ψ torsion angles determined via NCCN torsion angle measurements. [b]While both TALOS and NCCN analysis favor the listed torsion angles, there appears to be a secondary minimum with β-sheet-like torsion angles ($\phi \sim -80°$, $\psi \sim 117°$) that may also be consistent with our experimental data (see Figure S9 in the Supporting Information and main text below). [c]Results for N12 reflect the secondary structure identified by CSI analysis (Figure S4 in Supporting Information).

possibly consistent with IP β-sheets as in the crystals. If the simple model were not correct, and the labeled sites of one or more of the conformers were not sufficiently close and thus not contributing to the DQ buildup, we would expect the ^{13}C−^{13}C distance in the remaining conformers to be even shorter. For instance, simulations for two IP fibrillar peptide forms, and one that is antiparallel (with its ^{13}C′ sites too far apart to participate), yield an apparent distance of 4.7 Å for the parallel peptides (data not shown). Note that these measurements did not allow us to confirm that the intermolecular interactions involve the same or different conformers but do clearly show that the N-termini of at least some peptides must be close together. We address the uncertainties with additional intermolecular experiments.

We performed ^{13}C−^{13}C distance measurements via R^2 width (R^2W) experiments (*47*, *52*) on samples consisting of 50/50 (by mass) mixed ^{13}C′-Gly/^{13}Cα-Gly GNNQQNY fibril samples. In the mixed fibrils we measure intermolecular distances between labeled sites in neighboring peptides. For any peptide there is a 50% chance that its neighbor has the appropriate (i.e., different) labeling, in which case these intermolecular interactions would include two different closest distances (to peptides above and below) within the same β-sheet (see Figure 5e and Supporting Information). Figure 5c shows representative 2D panels from the R^2W experiment, near the polarization transfer maxima (where the MAS rate matches half the frequency difference between the selectively recoupled nuclei). The observed cross-peaks show that intermolecular polarization transfer occurs only between peptides of the same conformation (not between different conformers). Integration of cross-peak volumes as a function of the MAS rate yields R^2W profiles as shown in panel d. The maximum transfer occurs at different MAS rates (due to differences in chemical shift), but the maximum transfer is similar among the three fibril forms. Fits of these profiles yield ^{13}C−^{13}C distances of 4.5−4.9 (±1.0) Å for each of these fibril forms (see Table 5). These simulations assumed a single closest distance dominating the interaction as is the case in the monoclinic and orthorhombic crystal structures (Figure 5e). Note that the observed distance measurements are indeed consistent with the crystalline values, within the margin of error.

Figure 6 includes the results of REDOR-based intermolecular N−C distance measurements on a 57/43 (molar ratio) mixed ^{15}N-Gly/^{13}C′-Gly GNNQQNY fibril sample, showing significant dephasing due to the ^{15}N−^{13}C interaction. To check for any potential background dephasing, the experiment was also performed

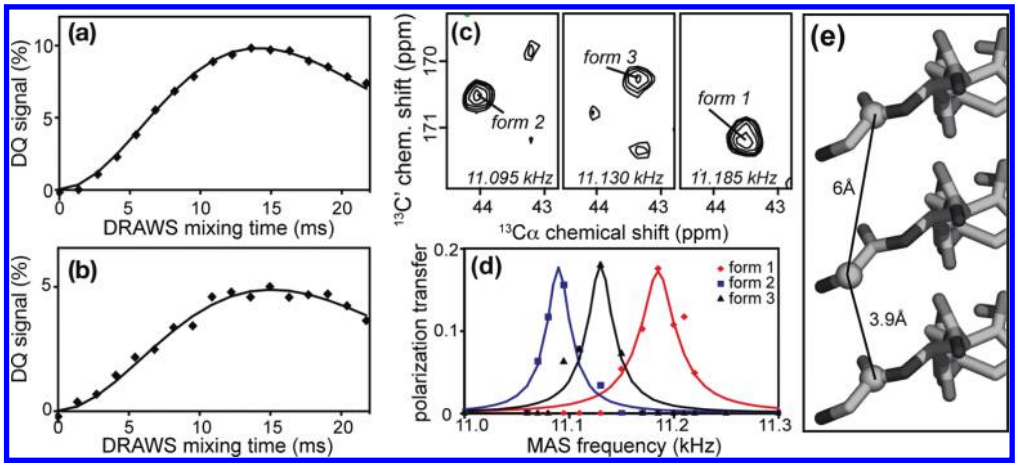

FIGURE 5: Intermolecular $^{13}C-^{13}C$ distance measurements. (a) DQ coherence buildup of G7-$^{13}C'$-labeled GNNQQNY monoclinic crystals, characteristic of their IP β-sheet structure. Diamonds indicate experimental values, and the solid line shows simulations for a 4.4 Å distance with 28 ms T_2 relaxation. (b) DQ buildup for G7-$^{13}C'$-labeled fibrils, showing the combined intensity of all three fibril forms, along with simulated data for a 4.9 Å $C'-C'$ distance and 16 ms T_2 relaxation. Both DRAWS experiments were done at $\omega_{0H}/2\pi = 500$ MHz with a MAS rate of 5.88 kHz. (c) 2D panels from R^2W experiments on 51/49 mixed G7-$^{13}C'$- and G7-$^{13}C\alpha$-labeled GNNQQNY fibrils at $\omega_{0H}/2\pi = 700$ MHz and 11.095, 11.130, and 11.185 kHz MAS frequencies. Cross-peaks reflect an intermolecular contact between the G7-C′ and G7-Cα and occur consistently within the same conformer. (d) Intermolecular R^2W profiles, where red diamonds, blue squares, and black triangles indicate experimental Cα intensities, normalized to the corresponding carbonyl peak volume. Solid lines indicate simulated R^2W profiles for distances of 4.5−4.9 (±1.0) Å. (e) Schematic showing the arrangement of the labeled Cα and C′ in the IP β-sheet of the monoclinic crystal structure.

Table 5: Overview of Intermolecular Distance Measurements[a]

	fibrils by MAS NMR				X-ray crystallography	
intermolecular distance	MAS NMR expt	conformer 1	conformer 2	conformer 3	monoclinic crystals	orthorhombic crystals
G7C′−G7C′	DRAWS[b]	4.9 ± 1.0 Å	4.9 ± 1.0 Å	4.9 ± 1.0 Å	4.9 Å	4.9 Å
G7C′−G7Cα	R^2W	4.5 ± 1.0 Å	4.85 ± 1.0 Å	4.7 ± 1.0 Å	3.9 Å	3.9 Å
G7C′−G7N	REDOR[c]	4.5 ± 0.8 Å	4.5 ± 0.6 Å	5.0 ± 0.8 Å	3.9 Å	4.0 Å

[a]Where applicable, distances between nonidentical sites (i.e., C′−Cα and C′−N contacts) only reflect the shorter distance of the two inequivalent pairings that characterize intrasheet contacts (see, e.g., Figure 5e). X-ray crystallographic distances are based on PDB files 1YJP and 2OMM, respectively (*4*, *5*). Note that the systematic errors listed reflect the assumptions made in the analysis, most notably assuming a lack of (undetermined) dynamical averaging, and sometimes do not account for all multispin interactions (see text and Supporting Information for specific details). The presence of significant molecular motion would imply shorter actual distances than listed. [b]Analysis assumed equivalent distance for all three fibril forms. [c]Results based on simple model with a single $^{13}C-^{15}N$ coupling.

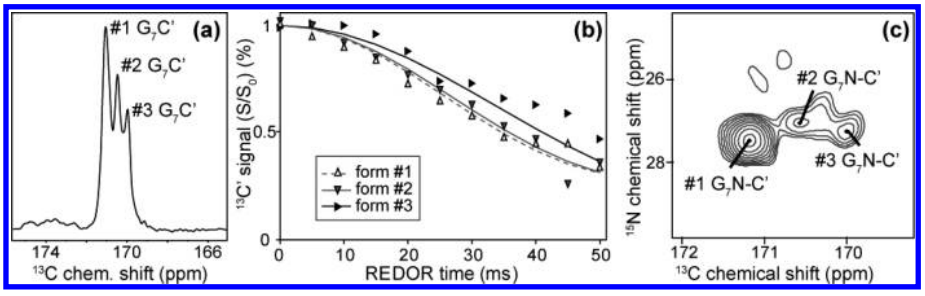

FIGURE 6: (a) 1D ^{13}C spectrum of $^{13}C'$-Gly-labeled GNNQQNY fibrils at $\omega_{H0}/2\pi = 700$ MHz and $\omega_r/2\pi = 10$ kHz showing the overlapping $^{13}C'$ signals from the three distinct conformers. (b) Experimental (triangles) and simulated (lines) REDOR dephasing curves from a 57/43 ^{15}N-Gly/$^{13}C'$-Gly mixed GNNQQNY fibril sample. These simulations correspond to $^{15}N-^{13}C$ distances of 4.6, 4.7, and 5.5 Å, respectively (see text for details). (c) 2D TEDOR spectrum showing form-specific cross-peaks within each fibril form (16 ms TEDOR mixing time).

on $^{13}C'$-Gly/$^{13}C\alpha$-Gly GNNQQNY fibrils (as used for the R^2W experiments). These data confirmed that none of the three fibril forms showed any significant background dephasing and thus that the observed REDOR dephasing is predominantly due to the labeled ^{15}N sites. These 1D REDOR data do not reveal which ^{13}C was dephased by which ^{15}N site. To examine this aspect, we recorded a 2D ZF-TEDOR spectrum with a 16 ms mixing time as shown in Figure 6c. It confirmed that each of the $^{13}C'$ sites interacts (only) with the ^{15}N site of the same fibril form, consistent with the R^2W data.

For a more quantitative analysis, the REDOR curves were simulated with SPINEVOLUTION. Initially, a simple simulation was performed where the interaction was described by a single $^{13}C-^{15}N$ coupling that accounts for the experimentally determined $^{15}N/^{13}C$ ratio. These distance fits suggest distances of 4.5 ± 0.8 Å, 4.5 ± 0.6 Å, and 5.0 ± 0.8 Å for the fibril conformers

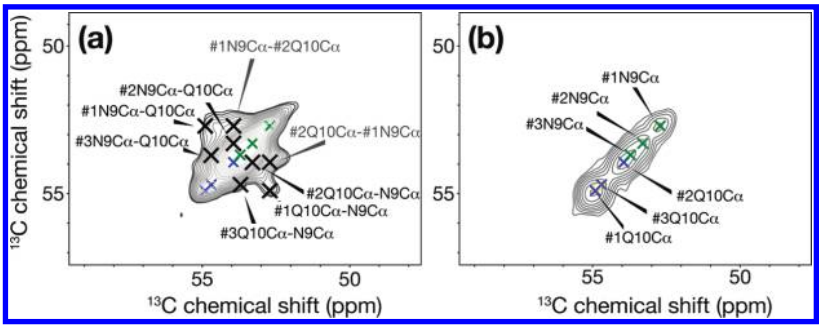

FIGURE 7: Cα−Cα segments of ^{13}C−^{13}C 2D spectra on a mixed GN[U-^{13}C,^{15}N-N]QQNY/GNN[U-^{13}C,^{15}N-Q]QNY fibril sample. (a) Experiment employing 14 ms ^{13}C−^{13}C PAR mixing at 9.5 kHz MAS rate and $\omega_{H0}/2\pi$ = 700 MHz. Several intermolecular cross-peaks can be observed between the backbone Cα's of N9 and Q10. Most reflect "intraform" contacts, similar to the results on G7. One interform (between conformers 1 and 2) contact is indicated in gray. (b) Same section from a 2D ^{13}C−^{13}C DARR experiment with 10 ms DARR mixing, showing the diagonal peaks along with their assignments ($\omega_r/2\pi$ = 9.5 kHz at $\omega_{H0}/2\pi$ = 700 MHz).

1, 2, and 3, respectively (Table 5). Note that in such a simulation we ignore the fact that there are multiple distance contributions to the interaction. To examine this aspect, we also tried a geometrical model that assumes an IP geometry (more details in the Supporting Information). The data do match this model, with the best fits shown in Figure 6b corresponding to ^{15}N−^{13}C distances of 4.6, 4.7, and 5.5 Å, respectively (with longer secondary distances of 6.2, 6.2, and 5.5 Å). We do note that under the constraints of this model the fit of the data achieved for the third conformer is not perfect. Since the N-termini could be less rigid, and we have seen some indications of increased motion (not shown), we tried simulations that included a limited amount of isotropic motional averaging (as a scaling of the dipolar interaction). These did yield improved fits to these form 3 data (data not shown). Generally, dynamics would imply actual distances that are shorter than our "rigid lattice" simulations suggest.

Intermolecular N9-Q10 Backbone Contacts. Additional data regarding intermolecular backbone contacts were obtained from a fibril sample prepared from a 50%/50% mixture of GN[U-^{13}C,^{15}N-N]-QQNY and GNN[U-^{13}C,^{15}N-Q]QNY. Here, any interresidue contacts should reflect intermolecular interactions. Such intermolecular contacts were indeed observed, including a number of backbone−backbone contacts that are of particular interest here. Figure 7a shows the Cα−Cα region of a ^{13}C−^{13}C PAR spectrum with τ_{mix} = 14 ms. Several interresidue, off-diagonal cross-peaks can be identified, based on our assignments and by comparison with shorter mixing time DARR data that show only the diagonal peaks (panel b). The internuclear distances associated with these contacts are harder to estimate than in the more quantitative measurements discussed earlier but should reflect distances of less than 7 Å (*61*). The figure also includes one interform cross-peak, which reflects the fact that we do actually observe interform contacts in this sample. Most of these involve side chain resonances and thus appear consistent with steric zipper-like interactions. However, due to the inherent ambiguity and signal overlap, their detailed analysis is beyond the scope of this publication. It necessitates additional complementary experimental data and is the topic of ongoing research but does suggest the possibility of interform polarization exchange, which implies an additional level of complexity in the GNNQQNY fibril assembly.

DISCUSSION

Fibril shifts. The newly determined chemical shift assignments in the C-terminal half of the peptide fibrils confirm a number of observations that we reported previously and also clarify some puzzling aspects of those results. Clearly, the shifts of the fibrils are different from the crystalline peptides throughout the length of the peptide (e.g., Figure 1 and Supporting Information Figure S3). Also, the conformational heterogeneity extends into these newly labeled residues, again showing three different sets of shifts. In this context, it is worth pointing out that these additional samples once again give the same resonances and intensity ratios as previously reported. Furthermore, we excluded the possibility that a preexisting seeding aggregate drives the polymorphism of these samples (which are sourced from different peptide syntheses from different companies) by filtering the freshly dissolved peptide through a 3 kDa cutoff centrifugal filter and again obtaining identical spectra with the same fibril forms (data not shown). One of those (conformer 2) previously diverged most strongly from the others, and its shifts appeared indicative of local helix-like backbone structure (*30*). However, based on the shifts themselves, the remaining residues in fibril form 2 appear to be β-sheet, indicating that the "helicity" is very localized. It was previously noted that there are apparent differences in the Tyr behavior in the crystals and fibrils, both from our NMR data and reported by others (*37*). Unfortunately, we did not label the Tyr residue (due to earlier synthetic difficulties). We can deduce some information on the Tyr shifts by comparison with limited spectral data from before, although not in a form-specific manner (see Figure S2 in Supporting Information). However, the Tyr shifts could not be included in the conformer-specific backbone analysis. A more detailed picture may be obtained from future NMR investigations.

Fibril Backbone Structure. We have used our MAS NMR data to determine the backbone structure of each of the three conformers present in the GNNQQNY amyloid fibrils. This was primarily motivated by the fact that the data indicated that one of the three coexisting fibril conformers might contain significant non-β structure (*30*). This was noteworthy since this is in contrast to the uniform β-sheet conformation of both GNNQQNY crystal structures and seemed counterintuitive in a short amyloid-forming peptide. Using more extensive labeling, extended chemical shift assignments, and explicit torsion angle measurements, we now provide a more complete and quantitative analysis of the backbone structure.

To examine any concerns regarding the applicability of TALOS and NCCN-based MAS NMR approaches to an amyloid fibril system (of such an unusually Q/N rich sequence), we took advantage of the availability of the crystal structures of known conformation. In agreement with our previous measurements (*30*, *84*),

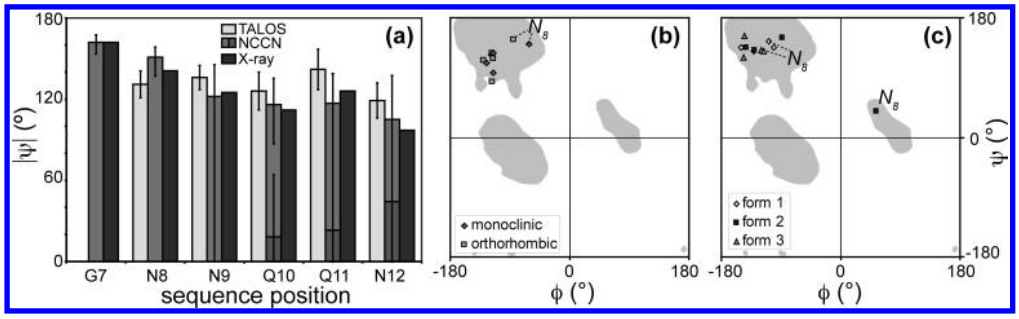

FIGURE 8: Torsion angle measurements. (a) Column graph comparing the TALOS and NCCN torsion angle results for the monoclinic GNNQQNY crystals to the angles obtained by X-ray crystallography (*4*). (b) Ramachandran plots of the GNNQQNY crystals, based on the X-ray results. The crystalline backbone angles fall within the β-sheet region (N12 is marked with open symbols). Each point represents a particular amino acid. (c) Torsion angles determined for the GNNQQNY fibrils (for residues N8−Q11). The fibril secondary structure shows a different distribution, with a significant deviation for the N-terminal residues of form 2. Overall, we see a structure composed primarily of β-sheet in the fibrils, based on our new MAS NMR data.

we find the TALOS program generates results in good agreement with the known torsion angles (Figure 8). We do note that the errors reported by TALOS appear to underestimate the actual deviations from the X-ray-based structures. There could be a number of factors that negatively affect the performance of TALOS in the samples at hand. One concern could be that the chemical shifts are affected by nonlocal contributions (e.g., the effect of nearby aromatic rings like the Tyr side chain on neighboring ^{13}C shifts (*85*)). In this context comparison of the chemical shifts of the two crystalline forms is of interest, since the monomers (in the X-ray structures) are virtually identical in structure, yet display significant differences in chemical shift. Based on the X-ray data, the heavy atom rmsd between the two crystal forms is 0.35 Å (0.26 Å for the backbone), as determined by the SUPERPOSE function in the CCP4 suite (*86*, *87*). The difference in chemical shift thus appears largely due to the difference in supramolecular packing of the monomers in the two crystal lattices. Another consideration in this particular comparison is that the X-ray data were obtained at 100 K, whereas the NMR chemical shifts are all obtained near room temperature, which may affect the structural and/or dynamical nature of the sample (*88*, *89*). Finally, the TALOS approach relies on the availability of segments of similar sequence and structure in the reference database, which may not be valid for these peptides.

Despite these potential concerns, the TALOS data from the crystals match the X-ray data with average deviations of 14−21° (see Supporting Information). We then examined the NCCN experiment and found its results to be quite accurate (see Figure 8a). While the NCCN torsion angles are consistent with the TALOS results, they do tend to represent an improvement in accuracy as the best-fit NCCN results match the X-ray data very well (see also Figure S7 in the Supporting Information). However, its precision can be limited, and it suffers from degeneracy in the fit solutions. In some cases the NCCN precision appears to be comparable to or inferior to the errors reported by TALOS. Recall, however, that the latter are likely to be underestimates (see Table S3 in the Supporting Information), whether due to features specific to these (solid) samples or in general (*90*).

For the fibrils we also applied such a combination of the NCCN and TALOS approaches, as summarized in Table 4. TALOS was unable to provide data for a number of residues (e.g., the N-terminal Gly and Asn-9 of conformer 2), and the NCCN torsion angle data provide insights into those residues. For a visual comparison, the results are plotted in panels b and c of Figure 8 in the form of Ramachandran plots (for the crystal residues 8−12 or residues 8−11 for the fibril conformers). The crystalline peptides have a uniform β-sheet structure, a feature that is reproduced in conformers 1 and 3. Fibril conformer 2, which previously showed some non-β structure (*30*), now is found to be largely β-sheet in terms of its backbone structure. A very notable distortion occurs near its N-terminus (Figure 8c), in a conformation that is somewhat reminiscent of a β-bulge conformation in terms of the backbone torsion angles (see Figure S14 in the Supporting Information for a schematic representation). Intriguingly, β-bulges have previously been suggested to prevent the lateral association of β-sheets (*91*, *92*). However, here the fibril appears to be able to accommodate this distorted backbone conformation within the β-sheets, perhaps analogous to amyloid-like crystals formed by the peptide MVGGVV derived from Aβ reported by Eisenberg and colleagues (*5*), which also feature a turn in the peptide backbone.

Intermolecular Arrangements. One of the key characteristics of the GNNQQNY crystal structures is the IP intrasheet alignment of the monomers. As pointed out by Sawaya et al. (*5*), both structures represent one out of many possible β-sheet configurations. We employed several independent measurements that showed intermolecular contacts between the N-terminal glycines, consistently only between peptides having the same conformation. In addition, we see intraform backbone−backbone contacts for each of the three fibril conformers in the long-mixing ^{13}C−^{13}C PAR experiments. Taken together, these data are consistent with, and even suggestive of, an IP alignment analogous to the crystalline aggregates. Especially with such short peptides in amyloid fibrils manifesting a multiplicity of conformations it is difficult to completely exclude all nonparallel and/or out-of-register sheet configurations, based on the current data. We note that the N-terminus is positively charged, as expected given the acidic conditions and confirmed by the ^{15}N chemical shift. This makes a very close proximity less desirable, but this tendency could be overcome by the extensive stabilizing interactions characteristic of the highly stable amyloid fibrils. This is indeed seen in several of the amyloid-like peptide crystal systems examined by Eisenberg and colleagues (*5*), as well as simulation studies on the GNNQQNY IP structure (*9*, *22*). Given the across-the-board intraform intermolecular interactions, the IP nature of both crystal forms (which form under very similar conditions and have even been reported to form from GNNQQNY fibrils (*37*)), the appearance that steric zipper features may be preserved in the fibrils (*30*), and the fact that various simulations find it to be the most stable alignment for GNNQQNY (*7*, *13*, *16*, *18*, *22*), we are

inclined to consider the MAS NMR results to strongly suggest a parallel in-register conformation. Note that seeing the intermolecular contacts only within a single conformer is specifically supportive of an IP β-sheet. Antiparallel β-sheets, as observed in crystals observed for other short peptides (*5*), tend to display structurally different monomers *within* the β-sheet, instead of the internally structurally identical, parallel β-sheets seen in both GNNQQNY crystal forms. Solid-state NMR studies of fibrils prepared from amylin fragments were found to be antiparallel within the β-sheets, as indicated by the detection of multiple sets of resonances of equal intensities (*93*). The latter observation also contrasts with the different intensities that characterize the different conformers detected in the GNNQQNY fibrils. Any antiparallel arrangement involving two of the fibril forms would necessitate equal populations for those conformers. Even though we have actually observed certain interform contacts in other experiments (such as the one indicated in Figure 7), these commonly involve side chains and are more consistent with steric zipper-like sheet-to-sheet contacts. However, those data on apparent sheet-to-sheet contacts necessitate a more detailed analysis and discussion that go beyond this publication.

If we compare the MAS NMR distance measurements to the equivalent distances in the crystal structures (Table 4), then we see that the measured distances in the fibrils tend to be slightly longer. However, these differences are within the margin of error of the experiments. There are several contributions that increase the uncertainty in these distances. First, the presence of multiple, partially overlapping conformers in all spectra makes it difficult to deconvolute the peaks. A second complication is related to the fact that the G7-labeled sites are near the peptide's N-terminus. This was done for practical reasons and related to the availability (and cost) of various singly labeled glycine variants (in contrast to appropriately backbone- and side chain-protected Gln, Asn, and Tyr). Since the Gly is near the N-terminus, increased dynamics may be expected (relative to the rest of the peptide). This is reflected in the temperature factors of the X-ray crystal structures (*4*, *5*) and simulations on GNNQQNY aggregates (*11*, *22*). Ongoing MAS NMR relaxation measurements suggest only moderate dynamics in the N-terminus and are the focus of a forthcoming publication. In any case, dynamics would effectively reduce the dipolar coupling and thus lead to *over*estimation of the distances. This would mean that the true distances might be shorter, therefore not changing the essence of our observed interactions or how they reflect on the supramolecular arrangement.

Experimentally, the observation of an IP β-sheet not only is reminiscent of the structure of the crystalline forms of GNNQQNY (*4*, *5*) but has also been observed in MAS NMR experiments on the parent protein Sup35p, Rnq1p, and fragments of Ure2p (*94*−*97*). All of these are Gln- and Asn-rich prion proteins found in yeast, but this pattern of IP β-sheet formation is quite common in amyloid fibrils in general and appears to facilitate amyloid formation in proteins of nonsymmetric (and purposely scrambled) primary sequences (*96*, *98*).

CONCLUSION

The GNNQQNY crystal structures have stimulated a great deal of interest as an atomic-level perspective of the core structure of amyloid fibrils. It also has spawned considerable research using *in silico* methods to further our understanding of the amyloid fibril formation and stability. The structural and mechanistic correlation between the crystalline and fibrillar aggregates has remained enigmatic, however, especially in the context of recent experimental data suggesting a transition between the fibrillar and crystalline conformations (*37*). We previously identified the presence of multiple conformations within the fibrils, which prominently included one with apparent non-β structure. We then also highlighted a number of indicators suggesting structural differences between the crystals and fibrils. Here we have presented new experimental data that explicitly address some of the key features of the crystal structures and reveal a number of basic similarities between the fibrils and crystals. Our data indicate that the conformers are actually all three predominantly β-sheet in structure but with a highly localized distortion in one of them. In addition, we have presented experimental data supporting a parallel, in-register assembly into form-specific β-sheets. These observations should serve as valuable experimental reference data to allow the continued development of GNNQQNY as an model amyloid system in theoretical studies. Conversely, given their independently known crystal structures, GNNQQNY (and other amyloid-like crystalline peptides) proved to be useful as an *experimental* amyloid test system for the development and demonstration of MAS NMR and other experimental techniques. Here we have used the crystalline form of the peptide as a reference system to examine the effectiveness of the TALOS analysis, NCCN torsion angle measurements, and $^{13}C-^{13}C$ distance measurements in a realistic amyloid-like β-sheet context of an independently known conformation.

Questions do remain regarding the role of these conformers within the fibrils. Such issues are the target of continued MAS NMR studies but will also benefit from experimentally informed *in silico* studies. For instance, it will be interesting to see whether a twisting or distortion of the peptide backbone is observed in fibrils assembled *in silico*. In the context of our results, theoretical studies may also be able to address the question of how the localized backbone twist (of conformer 2) may be accommodated into the fibrils and their seemingly IP β-sheet arrangement. As it is unclear whether this has been observed in the current computational studies, it may be important to more closely approximate the experimental conditions. In this regard, we point out that the concentration and pH appear to play critical roles that have not necessarily been sufficiently examined in the computational studies. Overall, our data point to an increased complexity in the behavior of the fibrillar form of GNNQQNY, even though it does share a variety of features with its crystals that continue to serve as a canonical model of the cross-β spine.

ACKNOWLEDGMENT

We thank Dr. Marc Caporini, Dr. Vikram Bajaj, and Dr. Marvin Bayro for help and feedback and gratefully acknowledge Dr. Mikhail Veshtort for providing the SPINEVOLUTION software. Molecular schematics were generated using Pymol (*99*).

SUPPORTING INFORMATION AVAILABLE

Assignment spectra, Tyr chemical shifts, and chemical shift comparisons to the crystals; CSI and TALOS data for the fibrils; additional experimental details on the MAS NMR experiments; additional details on the torsion angle data and analyses; schematics of the interstrand, intrasheet contacts in in-register parallel β-sheets; backbone schematics for the fibril conformers. This material is available free of charge via the Internet at http://pubs.acs.org.

REFERENCES

1. Chiti, F., and Dobson, C. M. (2006) Protein Misfolding, Functional Amyloid, and Human Disease. *Annu. Rev. Biochem. 75*, 333–366.
2. Langkilde, A. E., and Vestergaard, B. (2009) Methods for Structural Characterization of Prefibrillar Intermediates and Amyloid Fibrils. *FEBS Lett. 583*, 2600–2609.
3. Ma, B., and Nussinov, R. (2006) Simulations as Analytical Tools to Understand Protein Aggregation and Predict Amyloid Conformation. *Curr. Opin. Chem. Biol. 10*, 445–452.
4. Nelson, R., Sawaya, M. R., Balbirnie, M., Madsen, A. O., Riekel, C., Grothe, R., and Eisenberg, D. (2005) Structure of the Cross-Beta Spine of Amyloid-Like Fibrils. *Nature 435*, 773–778.
5. Sawaya, M. R., Sambashivan, S., Nelson, R., Ivanova, M. I., Sievers, S. A., Apostol, M. I., Thompson, M. J., Balbirnie, M., Wiltzius, J. J. W., McFarlane, H. T., Madsen, A. O., Riekel, C., and Eisenberg, D. (2007) Atomic Structures of Amyloid Cross-β Spines Reveal Varied Steric Zippers. *Nature 447*, 453–457.
6. Balbirnie, M., Grothe, R., and Eisenberg, D. S. (2001) An Amyloid-Forming Peptide from the Yeast Prion Sup35 Reveals a Dehydrated Beta-Sheet Structure for Amyloid. *Proc. Natl. Acad. Sci. U.S.A. 98*, 2375–2380.
7. Gsponer, J., Haberthür, U., and Caflisch, A. (2003) The Role of Side-Chain Interactions in the Early Steps of Aggregation: Molecular Dynamics Simulations of an Amyloid-Forming Peptide from the Yeast Prion Sup35. *Proc. Natl. Acad. Sci. U.S.A. 100*, 5154–5159.
8. Cecchini, M., Rao, F., Seeber, M., and Caflisch, A. (2004) Replica Exchange Molecular Dynamics Simulations of Amyloid Peptide Aggregation. *J. Chem. Phys. 121*, 10748–10756.
9. Lipfert, J., Franklin, J., Wu, F., and Doniach, S. (2005) Protein Misfolding and Amyloid Formation for the Peptide GNNQQNY from Yeast Prion Protein Sup35: Simulation by Reaction Path Annealing. *J. Mol. Biol. 349*, 648–658.
10. Fernández, A. (2005) What Factor Drives the Fibrillogenic Association of Beta-Sheets? *FEBS Lett. 579*, 6635–6640.
11. Zheng, J., Ma, B., Tsai, C.-J., and Nussinov, R. (2006) Structural Stability and Dynamics of an Amyloid-Forming Peptide GNNQQNY from the Yeast Prion Sup-35. *Biophys. J. 91*, 824–833.
12. Esposito, L., Pedone, C., and Vitagliano, L. (2006) Molecular Dynamics Analyses of Cross-Beta-Spine Steric Zipper Models: Beta-Sheet Twisting and Aggregation. *Proc. Natl. Acad. Sci. U.S.A. 103*, 11533–11538.
13. Zhang, Z., Chen, H., Bai, H., and Lai, L. (2007) Molecular Dynamics Simulations on the Oligomer-Formation Process of the GNNQQNY Peptide from Yeast Prion Protein Sup35. *Biophys. J. 93*, 1484–1492.
14. Wu, C., Wang, Z., Lei, H., Zhang, W., and Duan, Y. (2007) Dual Binding Modes of Congo Red to Amyloid Protofibril Surface Observed in Molecular Dynamics Simulations. *J. Am. Chem. Soc. 129*, 1225–1232.
15. Tsemekhman, K., Goldschmidt, L., Eisenberg, D., and Baker, D. (2007) Cooperative Hydrogen Bonding in Amyloid Formation. *Protein Sci. 16*, 761–764.
16. Strodel, B., Whittleston, C. S., and Wales, D. J. (2007) Thermodynamics and Kinetics of Aggregation for the GNNQQNY Peptide. *J. Am. Chem. Soc. 129*, 16005–16014.
17. Knowles, T. P., Fitzpatrick, A. W., Meehan, S., Mott, H. R., Vendruscolo, M., Dobson, C. M., and Welland, M. E. (2007) Role of Intermolecular Forces in Defining Material Properties of Protein Nanofibrils. *Science 318*, 1900–1903.
18. Meli, M., Morra, G., and Colombo, G. (2008) Investigating the Mechanism of Peptide Aggregation: Insights from Mixed Monte Carlo-Molecular Dynamics Simulations. *Biophys. J. 94*, 4414–4426.
19. De Simone, A., Esposito, L., Pedone, C., and Vitagliano, L. (2008) Insights into Stability and Toxicity of Amyloid-Like Oligomers by Replica Exchange Molecular Dynamics Analyses. *Biophys. J. 95*, 1965–1973.
20. Wang, J., Tan, C., Chen, H.-F., and Luo, R. (2008) All-Atom Computer Simulations of Amyloid Fibrils Disaggregation. *Biophys. J. 95*, 5037–5047.
21. Esposito, L., Paladino, A., Pedone, C., and Vitagliano, L. (2008) Insights into Structure, Stability, and Toxicity of Monomeric and Aggregated Polyglutamine Models from Molecular Dynamics Simulations. *Biophys. J. 94*, 4031–4040.
22. Vitagliano, L., Esposito, L., Pedone, C., and De Simone, A. (2008) Stability of Single Sheet GNNQQNY Aggregates Analyzed by Replica Exchange Molecular Dynamics: Antiparallel versus Parallel Association. *Biochem. Biophys. Res. Commun. 377*, 1036–1041.
23. Periole, X., Rampioni, A., Vendruscolo, M., and Mark, A. E. (2009) Factors That Affect the Degree of Twist in Beta-Sheet Structures: A Molecular Dynamics Simulation Study of a Cross-Beta Filament of the GNNQQNY Peptide. *J. Phys. Chem. B 113*, 1728–1737.
24. Berryman, J. T., Radford, S. E., and Harris, S. A. (2009) Thermodynamic Description of Polymorphism in Q- and N-Rich Peptide Aggregates Revealed by Atomistic Simulation. *Biophys. J. 97*, 1–11.
25. Reddy, G., Straub, J. E., and Thirumalai, D. (2009) Dynamics of locking of peptides onto growing amyloid fibrils. *Proc. Natl. Acad. Sci. U.S.A. 106*, 11948–11953.
26. Brovchenko, I., Singh, G., and Winter, R. (2009) Aggregation of Amyloidogenic Peptides near Hydrophobic and Hydrophilic Surfaces. *Langmuir 25*, 8111–8116.
27. Park, J., Kahng, B., and Hwang, W. (2009) Thermodynamic Selection of Steric Zipper Patterns in the Amyloid Cross-β Spine. *PLoS Comput. Biol. 5*, e1000492.
28. Glabe, C. G. (2008) Structural Classification of Toxic Amyloid Oligomers. *J. Biol. Chem. 283*, 29639–29643.
29. Diaz-Avalos, R., Long, C., Fontano, E., Balbirnie, M., Grothe, R., Eisenberg, D., and Caspar, D. L. D. (2003) Cross-beta order and diversity in nanocrystals of an amyloid-forming peptide. *J. Mol. Biol. 330*, 1165–1175.
30. Van der Wel, P. C. A., Lewandowski, J. R., and Griffin, R. G. (2007) Solid State NMR Study of Amyloid Nanocrystals and Fibrils Formed by the Peptide GNNQQNY from Yeast Prion Protein Sup35p. *J. Am. Chem. Soc. 129*, 5117–5130.
31. Jimenez, J. L., Guijarro, J. I., Orlova, E., Zurdo, J., Dobson, C. M., Sunde, M., and Saibil, H. R. (1999) Cryo-electron Microscopy Structure of an SH3 Amyloid Fibril and Model of the Molecular Packing. *EMBO J. 18*, 815–821.
32. Jimenez, J. L., Nettleton, E. J., Bouchard, M., Robinson, C. V., Dobson, C. M., and Saibil, H. R. (2002) The Protofilament Structure of Insulin Amyloid Fibrils. *Proc. Natl. Acad. Sci. U.S.A. 99*, 9196–9201.
33. Ferguson, N., Berriman, J., Petrovich, M., Sharpe, T. D., Finch, J. T., and Fersht, A. R. (2003) Rapid Amyloid Fiber Formation from the Fast-Folding WW Domain FBP28. *Proc. Natl. Acad. Sci. U.S.A. 100*, 9814–9819.
34. Saiki, M., Honda, S., Kawasaki, K., Zhou, D., Kaito, A., Konakahara, T., and Morii, H. (2005) Higher-Order Molecular Packing in Amyloid-Like Fibrils Constructed with Linear Arrangements of Hydrophobic and Hydrogen-Bonding Side-Chains. *J. Mol. Biol. 348*, 983–998.
35. Petkova, A. T., Leapman, R. D., Guo, Z., Yau, W.-M., Mattson, M. P., and Tycko, R. (2005) Self-Propagating, Molecular-Level Polymorphism in Alzheimer's β-Amyloid Fibrils. *Science 307*, 262–265.
36. Luca, S., Yau, W. M., Leapman, R., and Tycko, R. (2007) Peptide Conformation and Supramolecular Organization in Amylin Fibrils: Constraints from Solid-State NMR. *Biochemistry 46*, 13505–13522.
37. Marshall, K. E., Hicks, M. R., Williams, T. L., Hoffmann, S. V., Rodger, A., Dafforn, T. R., and Serpell, L. C. (2010) Characterizing the Assembly of the Sup35 Yeast Prion Fragment, GNNQQNY: Structural Changes Accompany a Fiber-to-Crystal Switch. *Biophys. J. 98*, 330–338.
38. Tycko, R. (2006) Molecular Structure of Amyloid Fibrils: Insights from Solid-State NMR. *Q. Rev. Biophys. 39*, 1–55.
39. Heise, H. (2008) Solid-State NMR Spectroscopy of Amyloid Proteins. *ChemBioChem 9*, 179–189.
40. Costa, P. R., Gross, J. D., Hong, M., and Griffin, R. G. (1997) Solid-State NMR Measurement of ψ in Peptides: a NCCN 2Q-Heteronuclear Local Field Experiment. *Chem. Phys. Lett. 280*, 95–103.
41. Gregory, D. M., Mitchell, D. J., Stringer, J. A., Kiihne, S., Shiels, J. C., Callahan, J., Mehta, M. A., and Drobny, G. P. (1995) Windowless Dipolar Recoupling: The Detection of Weak Dipolar Couplings between Spin 1/2 Nuclei with Large Chemical Shift Anisotropies. *Chem. Phys. Lett. 246*, 654–663.
42. Gregory, D. M., Benzinger, T. L. S., Burkoth, T. S., Miller-Auer, H., Lynn, D. G., Meredith, S. C., and Botto, R. E. (1998) Dipolar Recoupling NMR of Biomolecular Self-Assemblies: Determining Inter- And Intrastrand Distances in Fibrilized Alzheimer's β-Amyloid Peptide. *Solid State Nucl. Magn. Reson. 13*, 149–166.
43. Benzinger, T. L. S., Gregory, D. M., Burkoth, T. S., Miller-Auer, H., Lynn, D. G., Botto, R. E., and Meredith, S. C. (1998) Propagating Structure of Alzheimer's β-Amyloid$_{(10-35)}$ Is Parallel β-Sheet with Residues in Exact Register. *Proc. Natl. Acad. Sci. U.S.A. 95*, 13407–13412.
44. Caporini, M. A., Bajaj, V. S., Veshtort, M., Fitzpatrick, A., MacPhee, C. E., Vendruscolo, M., Dobson, C. M., and Griffin, R. G. (2010) Accurate Determination of Interstrand Distances and Alignment in Amyloid Fibrils by Magic Angle Spinning NMR. *J. Phys. Chem.*, in press.

45. Caporini, M. A. (2008) Structural Studies of Amyloid Fibrils Using Solid-State NMR, Ph.D. Thesis, Massachusetts Institute of Technology, Cambridge, MA.
46. Bajaj, V. S. (2007) Dynamic Nuclear Polarization in Biomolecular Solid State NMR: Methods and Applications in Peptides and Membrane Proteins, Ph.D. Thesis, Massachusetts Institute of Technology, Cambridge, MA.
47. Costa, P. R., Sun, B., and Griffin, R. G. (2003) Rotational Resonance NMR: Separation of Dipolar Coupling and Zero Quantum Relaxation. *J. Magn. Reson. 164*, 92–103.
48. Ramachandran, R., Ladizhansky, V., Bajaj, V. S., and Griffin, R. G. (2003) ^{13}C-^{13}C Rotational Resonance Width Distance Measurements in Uniformly ^{13}C-Labeled Peptides. *J. Am. Chem. Soc. 125*, 15623–15629.
49. Raleigh, D. P., Levitt, M. H., and Griffin, R. G. (1988) Rotational Resonance in Solid State NMR. *Chem. Phys. Lett. 146*, 71–76.
50. Colombo, M. G., Meier, B. H., and Ernst, R. R. (1988) Rotor-Driven Spin Diffusion in Natural-Abundance C-13 Spin Systems. *Chem. Phys. Lett. 146*, 189.
51. Levitt, M. H., Raleigh, D. P., Creuzet, F., and Griffin, R. G. (1990) Theory and Simulations of Homonuclear Spin Pair Systems in Rotating Solids. *J. Chem. Phys. 92*, 6347–6364.
52. Ramachandran, R., Lewandowski, J. R., van der Wel, P. C. A., and Griffin, R. G. (2006) Multipole Multimode Floquet Theory of Rotational Resonance Width Experiments: ^{13}C-^{13}C Distance Measurements in Uniformly Labeled Solids. *J. Chem. Phys. 124*, 214107.
53. van der Wel, P. C. A., Eddy, M. T., Ramachandran, R., and Griffin, R. G. (2009) Targeted ^{13}C-^{13}C Distance Measurements in a Microcrystalline Protein via J-Decoupled Rotational Resonance Width Measurements. *ChemPhysChem 10*, 1566–1663.
54. Barnes, A. B., Andreas, L. B., Huber, M., Ramachandran, R., van der Wel, P. C. A., Veshtort, M., Griffin, R. G., and Mehta, M. A. (2009) High-Resolution Solid-State NMR Structure of Alanyl-Prolyl-Glycine. *J. Magn. Reson. 200*, 95–100.
55. Gullion, T., and Schaefer, J. (1989) Rotational-Echo Double-Resonance NMR. *J. Magn. Reson. 81*, 196–200.
56. Hing, A. W., Vega, S., and Schaefer, J. (1992) Transferred-Echo Double-Resonance NMR. *J. Magn. Reson. 96*, 205–209.
57. Jaroniec, C. P., Filip, C., and Griffin, R. G. (2002) 3D TEDOR NMR Experiments for the Simultaneous Measurement of Multiple Carbon-Nitrogen Distances in Uniformly ^{13}C, ^{15}N-Labeled Solids. *J. Am. Chem. Soc. 124*, 10728–10742.
58. Madine, J., Jack, E., Stockley, P. G., Radford, S. E., Serpell, L. C., and Middleton, D. A. (2008) Structural Insights into the Polymorphism of Amyloid-Like Fibrils Formed by Region 20−29 of Amylin Revealed by Solid-State NMR and X-ray Fiber Diffraction. *J. Am. Chem. Soc. 130*, 14990–15001.
59. Gordon, D. J., Balbach, J. J., Tycko, R., and Meredith, S. C. (2004) Increasing the Amphiphilicity of an Amyloidogenic Peptide Changes the [Beta]-Sheet Structure in the Fibrils from Antiparallel to Parallel. *Biophys. J. 86*, 428–434.
60. Verel, R., Tomka, I. T., Bertozzi, C., Cadalbert, R., Kammerer, R. A., Steinmetz, M. O., and Meier, B. H. (2008) Polymorphism in an Amyloid-Like Fibril-Forming Model Peptide13. *Angew. Chem., Intl. Ed. 47*, 5842–5845.
61. De Paëpe, G., Lewandowski, J. R., Loquet, A., Böckmann, A., and Griffin, R. G. (2008) Proton Assisted Recoupling and Protein Structure Determination. *J. Chem. Phys. 129*, 245101.
62. Stringer, J. A., Bronnimann, C. E., Mullen, C. G., Zhou, D. H., Stellfox, S. A., Li, Y., Williams, E. H., and Rienstra, C. M. (2005) Reduction of RF-Induced Sample Heating with a Scroll Coil Resonator Structure for Solid-State NMR Probes. *J. Magn. Reson. 173*, 40–48.
63. Takegoshi, K., Nakamura, S., and Terao, T. (2001) C-13-H-1 Dipolar-Assisted Rotational Resonance in Magic-Angle Spinning NMR. *Chem. Phys. Lett. 344*, 631–637.
64. Morcombe, C. R., Gaponenko, V., Byrd, R. A., and Zilm, K. W. (2004) Diluting Abundant Spins by Isotope Edited Radio Frequency Field Assisted Diffusion. *J. Am. Chem. Soc. 126*, 7196–7197.
65. Lewandowski, J., De Paëpe, G., and Griffin, R. G. (2007) Proton Assisted Insensitive Nuclei Cross Polarization. *J. Am. Chem. Soc. 129*, 728–729.
66. Schaefer, J., McKay, R. A., and Stejskal, E. O. (1979) Double-Cross-Polarization NMR of Solids. *J. Magn. Reson. 34*, 443–447.
67. Baldus, M., Petkova, A. T., Herzfeld, J., and Griffin, R. G. (1998) Cross Polarization in the Tilted Frame: Assignment and Spectral Simplification in Heteronuclear Spin Systems. *Mol. Phys. 95*, 1197–1207.
68. Petkova, A. T., Baldus, M., Belenky, M., Hong, M., Griffin, R. G., and Herzfeld, J. (2003) Backbone and Side Chain Assignment Strategies for Multiply Labeled Membrane Peptides and Proteins in the Solid State. *J. Magn. Reson. 160*, 1–12.
69. Egorova-Zachernyuk, T. A., Hollander, J., Fraser, N., Gast, P., Hoff, A. J., Cogdell, J., de Groot, H. J. M., and Baldus, M. (2001) Heteronuclear 2D-Correlations in a Uniformly [^{13}C, ^{15}N] Labeled Membrane-Protein Complex at Ultra-High Magnetic Fields. *J. Biomol. NMR 19*, 243–253.
70. Pauli, J., Baldus, M., van Rossum, B.-J., de Groot, H. J. M., and Oschkinat, H. (2001) Backbone and Side-Chain ^{13}C and ^{15}N Signal Assignments of the α-Spectrin SH3 Domain by Magic Angle Spinning Solid-State NMR at 17.6 T. *ChemBioChem 2*, 272–281.
71. Bennett, A. E., Rienstra, C. M., Auger, M., Lakshmi, K. V., and Griffin, R. G. (1995) Heteronuclear Decoupling in Rotating Solids. *J. Chem. Phys. 103*, 6951–6957.
72. Morcombe, C. R., and Zilm, K. W. (2003) Chemical Shift Referencing in MAS Solid State NMR. *J. Magn. Reson. 162*, 479–486.
73. Markley, J. L., Bax, A., Arata, Y., Hilbers, C. W., Kaptein, R., Sykes, B. D., Wright, P. E., and Wüthrich, K. (1998) Recommendations for the Presentation of NMR Structures of Proteins and Nucleic Acids. *Pure Appl. Chem. 70*, 117–142.
74. Harris, R. K., Becker, E. D., Cabral de Menezes, S. M., Goodfellow, R., and Granger, P. (2002) NMR Nomenclature: Nuclear Spin Properties and Conventions for Chemical Shifts. *Solid State Nucl. Magn. Reson. 22*, 458–483.
75. Delaglio, F., Grzesiek, S., Vuister, G. W., Zhu, G., Pfeifer, J., and Bax, A. (1995) NMRPipe: a Multidimensional Spectral Processing System Based on UNIX Pipes. *J. Biomol. NMR 6*, 277–293.
76. Goddard, T. D., and Kneller, D. G. (2006) SPARKY 3, University of California, San Francisco.
77. Vranken, W. F., Boucher, W., Stevens, T. J., Fogh, R. H., Pajon, A., Llinas, M., Ulrich, E. L., Markley, J. L., Ionides, J., and Laue, E. D. (2005) The CCPN Data Model for NMR Spectroscopy: Development of a Software Pipeline. *Proteins: Struct., Funct., Bioinf. 59*, 687–696.
78. Cornilescu, G., Delaglio, F., and Bax, A. (1999) Protein Backbone Angle Restraints from Searching a Database for Chemical Shift and Sequence Homology. *J. Biomol. NMR 13*, 289–302.
79. Feng, X., Lee, Y. K., Sandström, D., Eden, M., Maisel, H., Sebald, A., and Levitt, M. H. (1996) Direct Determination of a Molecular Torsional Angle by Solid-State NMR. *Chem. Phys. Lett. 257*, 314–320.
80. Hohwy, M., Rienstra, C. M., Jaroniec, C. P., and Griffin, R. G. (1999) Fivefold Symmetric Homonuclear Dipolar Recoupling in Rotating Solids: Application to Double Quantum Spectroscopy. *J. Chem. Phys. 110*, 7983–7992.
81. Veshtort, M., and Griffin, R. G. (2006) SPINEVOLUTION: A Powerful Tool for the Simulation of Solid and Liquid State NMR Experiments. *J. Magn. Reson. 178*, 248–282.
82. Wishart, D. S., and Sykes, B. D. (1994) The ^{13}C Chemical-Shift Index: A Simple Method for the Identification of Protein Secondary Structure Using ^{13}C Chemical-Shift Data. *J. Biomol. NMR 4*, 171–180.
83. Zhang, H., Neal, S., and Wishart, D. S. (2003) RefDB: A Database of Uniformly Referenced Protein Chemical Shifts. *J. Biomol. NMR 25*, 173–195.
84. Jaroniec, C. P., MacPhee, C. E., Astrof, N. S., Dobson, C. M., and Griffin, R. G. (2002) Molecular Conformation of a Peptide Fragment of Transthyretin in an Amyloid Fibril. *Proc. Natl. Acad. Sci. U.S.A. 99*, 16748–16753.
85. Ma, Z., Halling, M. D., Solum, M. S., Harper, J. K., Orendt, A. M., Facelli, J. C., Pugmire, R. J., Grant, D. M., Amick, A. W., and Scott, L. T. (2007) Ring Current Effects in Crystals. Evidence from ^{13}C Chemical Shift Tensors for Intermolecular Shielding in 4,7-Di-t-butylacenaphthene versus 4,7-Di-t-butylacenaphthylene. *J. Phys. Chem. A 111*, 2020–2027.
86. Krissinel, E., and Henrick, K. (2004) Secondary-Structure Matching (SSM), a New Tool for Fast Protein Structure Alignment in Three Dimensions. *Acta Crystallogr. D 60*, 2256–2268.
87. Collaborative Computational Project Number 4 (1994) The CCP4 Suite: Programs for Protein Crystallography. *Acta Crystallogr. D 50*, 760–763.
88. Bajaj, V. S., van der Wel, P. C. A., and Griffin, R. G. (2008) Observation of a Low-Temperature, Dynamically Driven Structural Transition in a Polypeptide by Solid-State NMR Spectroscopy. *J. Am. Chem. Soc. 131*, 118–128.
89. Debelouchina, G. T., Bayro, M. J., Van Der Wel, P. C. A., Caporini, M. A., Barnes, A. B., Rosay, M., Maas, W. E., and Griffin, R. G. (2010) Dynamic Nuclear Polarization-Enhanced Solid-State NMR Spectroscopy of GNNQQNY Nanocrystals and Amyloid Fibrils. *Phys. Chem. Chem. Phys.* 1–11.

90. Cheung, M.-S., Maguire, M. L., Stevens, T. J., and Broadhurst, R. W. (2010) DANGLE: A Bayesian Inferential Method for Predicting Protein Backbone Dihedral Angles and Secondary Structure. *J. Magn. Reson. 202*, 223–233.
91. Richardson, J. S., and Richardson, D. C. (2002) Natural Beta-Sheet Proteins Use Negative Design to Avoid Edge-to-Edge Aggregation. *Proc. Natl. Acad. Sci. U.S.A. 99*, 2754–2759.
92. De Simone, A., Dodson, G. G., Fraternali, F., and Zagari, A. (2006) Water Molecules As Structural Determinants among Prions of Low Sequence Identity. *FEBS Lett. 580*, 2488–2494.
93. Nielsen, J. T., Bjerring, M., Jeppesen, M. D., Pedersen, R. O., Pedersen, J. M., Hein, Kim L., Vosegaard, T., Skrydstrup, T., Otzen, D. E., and Nielsen, N. C. (2009) Unique Identification of Supramolecular Structures in Amyloid Fibrils by Solid-State NMR Spectroscopy. *Angew. Chem., Intl. Ed. 48*, 2118–2121.
94. Shewmaker, F., Kryndushkin, D., Chen, B., Tycko, R., and Wickner, R. B. (2009) Two Prion Variants of Sup35p Have In-Register Parallel Beta-Sheet Structures, Independent of Hydration. *Biochemistry 48*, 5074–5082.
95. Wickner, R. B., Dyda, F., and Tycko, R. (2008) Amyloid of Rnq1p, the Basis of the [PIN+] Prion, Has a Parallel In-Register Beta-Sheet Structure. *Proc. Natl. Acad. Sci. U.S.A. 105*, 2403–2408.
96. Baxa, U., Wickner, R. B., Steven, A. C., Anderson, D. E., Marekov, L. N., Yau, W.-M., and Tycko, R. (2007) Characterization of Beta-Sheet Structure in Ure2p1−89 Yeast Prion Fibrils by Solid-State Nuclear Magnetic Resonance. *Biochemistry 46*, 13149–13162.
97. Shewmaker, F., Wickner, R. B., and Tycko, R. (2006) Amyloid of the Prion Domain of Sup35p Has an In-Register Parallel Beta-Sheet Structure. *Proc. Natl. Acad. Sci. U.S.A. 103*, 19754–19759.
98. Ross, E. D., Minton, A., and Wickner, R. B. (2005) Prion Domains: Sequences, Structures and Interactions. *Nat. Cell Biol. 7*, 1039–1044.
99. DeLano, W. L. (2002) The PyMOL Molecular Graphics System, DeLano Scientific, San Carlos, CA.